ACCSCIENCE PUBLISHING

Journal of Seismic Exploration

ARTICLE

Direct envelope-based reflection full waveform inversion for shallow marine seismic data

Kyoungmin Lim[1], Wookeen Chung[1], Jungkyun Shin[2], and Jiho Ha[2]*

[1]Department of Energy and Resources Engineering, National Korea Maritime & Ocean University, Busan, Republic of Korea

[2]Pohang Research Branch, Korea Institute of Geoscience and Mineral Resources, Pohang, Republic of Korea

(This article belongs to the *Special Issue: Full Waveform Inversion Methods and Applications for Seismic Data in Complex Media*)

Abstract

Accurate velocity models that include long-wavelength components are required for precise subsurface structure imaging and estimation of geophysical properties. To successfully build the long-wavelength velocity using full waveform inversion (FWI), sufficient offset and low-frequency components are necessary. However, due to the limited acquisition conditions, it is difficult to operate long offset and low-frequency sources in coastal shallow marine. Short offset makes the data dominated by reflections, and FWI intensively updates the surface boundaries. Although reflection full waveform inversion (RFWI) has been proposed to reconstruct long-wavelength velocity models using reflection data, it suffers from cycle skipping when low-frequency component is insufficient. To overcome these limitations, we propose a direct envelope-based RFWI (DE-RFWI) that incorporates the direct envelope into the RFWI. By employing envelope-based energy information from reflection data, DE-RFWI facilitates the reconstruction of long-wavelength velocity. The proposed method employs the Hilbert transform-based implicit gradient decomposition technique to address additional computational cost. To verify the proposed method, DE-RFWI was applied to synthetic test with a shallow marine condition and field data acquired in Yeongil Bay, South Korea. The inversion results for field data were evaluated by analyzing arrival-time alignment in envelope domain. The results demonstrate that DE-RFWI can reliably reconstruct long-wavelength velocity models in shallow marine seismic data and improve reflector continuity and resolution in the reverse time migration imaging.

Keywords: Long-wavelength velocity model; Shallow marine seismic; Short offset; Reflection full waveform inversion; Direct envelope

***Corresponding author:**
Jiho Ha
(jihoha@kigam.re.kr)

Citation: Lim K, Chung W, Shin J, Ha J. Direct envelope-based reflection full waveform inversion for shallow marine seismic data. *J Seismic Explor*. 2026;35(2):026030005. doi: 10.36922/JSE026030005

Received: January 14, 2026

Revised: February 25, 2026

Accepted: March 9, 2026

Published online: March 27, 2026

Copyright: © 2026 Author(s). This is an Open-Access article distributed under the terms of the Creative Commons Attribution License, permitting distribution, and reproduction in any medium, provided the original work is properly cited.

Publisher's Note: AccScience Publishing remains neutral with regard to jurisdictional claims in published maps and institutional affiliations.

1. Introduction

Recently, increasing interest in coastal regions, such as the offshore wind farms, stability assessment of marine structures, submarine geological monitoring, and geo-hazard detection, has highlighted the growing need for accurate characterization of

subsurface elastic properties and velocity structures. Multi-beam echo sounder (MBES) and sub-bottom profiler (SBP) are survey systems widely used in coastal region. Since MBES and SBP operate at high frequencies, these systems provide only information on the seafloor and the shallow subsurface.[1-3] In contrast, marine seismic surveys that use air-gun and sparker cover a frequency range within the tens-of-hertz to kilohertz band, providing information on deeper subsurface structures. However, conventional seismic survey for reservoir exploration requires long streamer arrays and large vessels, limiting their applicability in coastal areas where the water depth is shallow and various fishing activities are conducted. To overcome these challenges, ultra-high resolution (UHR) seismic survey has been adopted.[4,5] UHR surveys can be operated from small vessels, reduce the group interval, and utilize higher source frequencies, enabling the acquisition of high-resolution seismic data.

Seismic signals acquired in coastal shallow marine are dominantly recorded as reflections because the short source-receiver offset restrict the propagation paths. Although this characteristic enhances the resolution of seismic sections, it suffers from a lack of wide-aperture. Wide-aperture signals are crucial for velocity model building and have been utilized to reconstruct long-wavelength components of the subsurface structure.[6-9]

Full waveform inversion (FWI) is a technique that estimates high-resolution subsurface properties by minimizing the misfit between modeled and observed waveforms. Under ideal conditions, FWI can update both subsurface reflectors and the background velocity, which are controlled by the migration and tomography components, respectively.[10] However, because FWI relies on wide-aperture information to build a long-wavelength velocity model,[11,12] it becomes challenging to obtain a reliable long-wavelength model on reflection dominant data.

In reflection dominant data, the migration component is much stronger than the tomography component, resulting in boundary-limited updates. Reflection full waveform inversion (RFWI) was proposed[13] to recover long-wavelength velocity model with reflection data. Table 1 summarizes representative prior studies on RFWI, classified according to their primary research focus. The Freq. and Max. offset columns describe the data specifications used in the numerical tests. The frequency not given as a range denotes the dominant frequency. Early studies recognized that gradient derived from reflection data is migration dominant, and gradient decomposition strategies were introduced to enhance the tomographic component.[13-17] More recently, RFWI has been extended to elastic and anisotropic media,[18-20] and efforts have been made to improve its computational efficiency.[21-23]

To enhance the tomographic component in reflection data, Xu *et al.*[13] decomposed the gradient into migration and tomography component by separating the incident and scattered wavefields using a Born modeling. Born modeling-based approaches have been widely used because the first-order scattered wavefield can be explicitly isolated.[24-26] However, such approaches are based on the Born approximation to simulate the first order scattering, and it is difficult to account for higher-order scattering effects.[27] Wavefield decomposition methods separate the source and receiver wavefields into up/down-going according to their propagation directions, from which the migration and tomography components can be constructed. This strategy can effectively separate each component in shallow seismic conditions where wave propagation is relatively simple and clear. Therefore, in this study, we adopted a wavefield decomposition method to separate the migration and tomography components.

RFWI can reconstruct long-wavelength velocity models using reflection data. However, because conventional RFWI employs the waveform matching–based objective function, it becomes vulnerable to cycle skipping and local minima.[25] To mitigate this issue, the correlation-based objective function that emphasizes kinematic similarity[28] and envelope-based objective function that suppresses phase dependence[29,30] were proposed. However, conventional envelope inversion calculates the waveform-based Fréchet derivative through the chain rule, and the gradient can be distorted in the reflection data. To overcome these issues, Wu and Chen[31] proposed direct envelope inversion (DEI), which can stably estimate long-wavelength velocity under strong scattering conditions by directly deriving the envelope Fréchet derivative. DEI has been successfully applied to reconstruct large-scale velocity anomalies with strong velocity contrasts.[32-34]

Chen *et al.*[29] demonstrated that multi-scale DEI prior to multi-scale RFWI leads to reliable long-wavelength velocity model and improves subsalt imaging. They applied wavefield decomposition to DEI, in which the migration and tomography components were alternately utilized to update the short- and long-wavelength components, respectively. Although their approach achieved successful results in synthetic experiments, the decomposition method in f-k domain requires storing both source and receiver wavefields at every time steps, resulting in large memory consumption. This limitation becomes more critical in shallow marine seismic data, where high-frequency data and dense temporal samples are required. Therefore, in this study, we adopt an efficient wavefield decomposition

technique based on the Hilbert transform proposed by Lian *et al.*[35] This method can implicitly decompose the wavefields in time-space domain by constructing analytic signals using the Hilbert transform to separate up/down-going components. Since each component can be implicitly extracted in time-space domain, 2D FFT is unnecessary to transform f - k domain and storing the full wavefields can be avoided.

Previous RFWI studies have generally been conducted using datasets with offsets of several kilometers and frequency bands below several tens of hertz. Although short-offset targeted study has been reported,[36] it still relied on offset ranges exceeding 1 km. In this study, we aim to reconstruct a long-wavelength velocity model from shallow marine seismic data. Accordingly, the RFWI is proposed to recover long-wavelength velocity information from reflection dominant data. Shallow seismic data are characterized by severely limited offsets and the difficulty of utilizing low-frequency sources, resulting in wavefields dominated by strong boundary reflections. These characteristics are similar to the strong-scattering

Table 1. Representative prior studies on RFWI

Category	Year	Authors	Remarks	Freq.	Max. offset
Gradient decomposition	2012	Xu *et al.*[13]	Proposed the RFWI to recover the long-wavelength velocity model from reflected waves	~8 Hz	8 km
	2013	Tang *et al.*[14]	Decomposed the gradient into tomography and migration components and emphasized the tomography component using weight factor	25 Hz	-
	2014	Alkhalifah[15]	Proposed the scattering-angle-guided filter for gradient decomposition	-	-
	2016	Wang *et al.*[16]	Proposed the alternating inversion of long- and short-wavelength components using wavefield decomposition	5–40 Hz	1.2 km
	2018	Yao *et al.*[17]	Proposed the plane-wave angle filter to separate migration and tomography components	~24 Hz	10 km
Objective function	2015	Chi *et al.*[28]	Introduced the correlation-based objective function for RFWI	-	3.875 km
	2015	Wu & Alkhalifah[37]	Proposed simultaneous inversion of background and perturbation using modified objective function	-	-
	2018	Chen *et al.*[29]	Proposed the multi-scale envelope inversion using WAE to construct start model of multi-scale RFWI	4–40 Hz	7 km
	2024	Wang *et al.*[30]	Proposed the envelope-normalized objective function for RFWI	-	4 km
	2026	**Lim *et al.* (this paper)**	**Proposed the direct envelope-based RFWI to reconstruct long-wavelength velocity model on shallow marine seismic data**	**~200 Hz**	**90 m**
Elastic media	2017	Guo & Alkhalifah[18]	Introduced the elastic RFWI to update P and S long-wavelength velocity using equivalent stress source	2–8 Hz	6 km
Anisotropy	2020	Li & Alkhalifah[19]	Proposed the multi-parameter RFWI for acoustic VTI media	2–8 Hz	3 km
	2023	Wu *et al.*[20]	Introduced the Gauss–Newton multi-parameter RFWI for VTI media.	5–25 Hz	4 km
Computational efficiency	2021	Song & Alkhalifah[21]	Introduced EWI using subsurface secondary source into RFWI to improve computational efficiency	3–10 Hz	3 km
	2021	Wang *et al.*[22]	Proposed the matrix-free Gauss–Newton RFWI to improve convergence speed	6–25 Hz	8 km
	2022	Xu *et al.*[23]	Proposed the second-order Gauss–Newton optimization to RFWI to improve convergence speed and resolution	-	4 km

Abbreviations: EWI: Efficient wavefield inversion; RFWI: Reflection full waveform inversion; VTI: Vertical transversely isotropic; WAE: Window-averaged envelope.

conditions assumed in DEI.

Based on these similarities, we propose a direct envelope–based RFWI (DE-RFWI) strategy that incorporates DEI into the RFWI to reconstruct long-wavelength velocity models from shallow marine seismic data. RFWI is adopted to overcome the insufficient wide-aperture information due to limited offset, and DEI is employed to mitigate low-frequency component deficiency and phase sensitivity. The effectiveness of the DE-RFWI approach is demonstrated through numerical examples, and its applicability is further validated using field data.

2. Methodology

2.1 Full waveform inversion (FWI)

Full waveform inversion (FWI) reconstructs high-resolution subsurface properties by minimizing the misfit between modeled and observed data. Because FWI exploits both the amplitude and phase of the entire waveform, it is capable of estimating velocity models. FWI is formulated as an optimization problem that minimizes the following misfit function:[38]

$$J(\mathbf{m}) = \frac{1}{2}\sum_{s}\sum_{r}\int\left[u(t,m,r;s) - d(t,r;s)\right]^2 dt \tag{1}$$

where u is modeled data and d is observed data with s and r indicating the locations of source and receiver. The gradient can be calculated by taking a partial derivative with respect to the model parameters $\mathbf{m}$:

$$\mathrm{g} = \frac{\partial J(\mathbf{m})}{\partial \mathbf{m}} = \sum_{s}\sum_{r}\int \frac{\partial u(t,r;s)}{\partial \mathbf{m}} \cdot R(t,r;s)\,dt \tag{2}$$

where g is gradient, $(\partial u/\partial \mathbf{m})$ is the partial derivative wavefield, and $R = u - d$ is residual between modeled data and observed data, and $\cdot$ indicates the dot product operator. The partial derivative wavefield can be expressed by using the Green's function $\mathbf{G}$ and virtual source wavefield $\mathbf{v}$:[39]

$$\frac{\partial u}{\partial \mathbf{m}} = \mathbf{G}(t) * \mathbf{v}(t) = \mathbf{v}(t) * \mathbf{G}(t) \tag{3}$$

where $*$ is a convolution operator in time. By substituting **Equation 3** into **Equation 2**, the gradient can be written as:

$$\begin{aligned} g &= \sum_{s}\sum_{r}\left(\mathbf{v}(t) * \mathbf{G}(t)\right) \cdot R(t,r;s) \\ &= \sum_{s}\sum_{r}\mathbf{v}(t) * \left(\mathbf{G}(t) * R(T_{max} - t, r;s)\right) \\ &= \sum_{s}\sum_{r}\mathbf{v}(t) * \mathbf{B}(t) \end{aligned} \tag{4}$$

where $\mathbf{B}$ is the back-propagated wavefield calculated by propagating the time-reverse residual wavefield.

2.2. Reflection full waveform inversion (RFWI)

When sufficient offset and broad frequency bandwidth are available, FWI can effectively recover not only reflector boundaries through the migration component but also the background velocity through the tomography component.[10] However, in limited offset conditions, FWI performs updates primarily along boundaries. In the absence of wide-aperture energy, most of the recorded signals consist of reflections. The reflection kernel in FWI appears as a mixture of the oval-shaped migration and the rabbit-ear-shaped tomography component (Figure 1A). Because the migration component is much stronger than tomography component, FWI applied to reflection data fails to reconstruct the background velocity.

To overcome this limitation, Xu *et al.*[13] proposed RFWI, which can stably update the long-wavelength velocity model by selectively utilizing tomography components. By separating migration and tomography components from the full reflection kernel, each component can be independently emphasized. Figure 1B shows the highlights of the oval-shaped migration component, whereas Figure 1C presents the rabbit-ear-shaped tomography component with weakened migration component. The essential concept of RFWI is to decompose the tomography component, which contains long-wavelength information.[27]

A wavefield can be separated into up/down-going according to the propagation direction, which can be explicitly decomposed in the frequency-wavenumber domain by performing a two-dimensional fast Fourier transform (2D FFT) as follows:[40]

$$u(\omega,k_z) = \begin{cases} u_u(\omega,k_z), if\ \omega k_z < 0 \\ u_d(\omega,k_z), if\ \omega k_z \geq 0 \end{cases} \tag{5}$$

where u_u is the up-going wavefield and u_d is the down-going wavefield. From **Equation 4**, the migration and tomography components can be expressed by combining the decomposed wavefields:

$$\mathrm{g}_{mig} = \sum_{s}\sum_{r}\mathbf{v}_u(t) * \mathbf{B}_d(t) + \mathbf{v}_d(t) * \mathbf{B}_u(t) \tag{6}$$

$$\mathrm{g}_{tomo} = \sum_{s}\sum_{r}\mathbf{v}_u(t) * \mathbf{B}_u(t) + \mathbf{v}_d(t) * \mathbf{B}_d(t) \tag{7}$$

However, the explicit decomposition method in the f-k domain requires storing the wavefield at every time step, which leads to high memory cost. Figure 2 depicts the wavefield decomposition performed in f-k domain, where repetitive 2D FFT and IFFT computations on every z-t wavefield slice are required. In particular, this limitation becomes critical in shallow seismic applications, where high-frequency content requires dense temporal samples. To overcome this, we adopted an implicit

wavefield decomposition method proposed by Lian *et al.*,[35] which can be implemented in the time-space domain. Implicit decomposition method constructs a complex wavefield by applying Hilbert transforms in both the time and depth directions. For a wavefield $u(z,t)$, the complex wavefield $\tilde{u}(z,t)$ calculated by applying the temporal Hilbert transform $\mathcal{H}_t$ is defined as follows:[41]

$$\tilde{u}(z,t) = u(z,t) + i\mathcal{H}_t\left[u(z,t)\right] \tag{8}$$

By applying an additional Hilbert transform $\mathcal{H}_z$ in the depth direction, the wavefield can be separated by:[35]

$$\begin{aligned} u_u(z,t) &= \frac{1}{2}\left[\tilde{u}(z,t) + i\mathcal{H}_z\left[\tilde{u}(z,t)\right]\right] \\ u_d(z,t) &= \frac{1}{2}\left[\tilde{u}(z,t) - i\mathcal{H}_z\left[\tilde{u}(z,t)\right]\right] \end{aligned} \tag{9}$$

Therefore, based on **Equation 9**, **Equations 6** and **7** can be rewritten as follows:

$$\mathrm{g}_{mig} = \sum_s\sum_r 2\left[\mathbf{v}(t) * \mathbf{B}(t) + \mathcal{H}_z\left[\mathbf{v}(t)\right] * \mathcal{H}_z\left[\mathbf{B}(t)\right]\right] \tag{10}$$

$$\mathrm{g}_{tomo} = \sum_s\sum_r 2\left[\mathbf{v}(t) * \mathbf{B}(t) - \mathcal{H}_z\left[\mathbf{v}(t)\right] * \mathcal{H}_z\left[\mathbf{B}(t)\right]\right] \tag{11}$$

Based on **Equations 10** and **11**, the process of combining the up/down going wavefields (**Equations 6** and **7**) can be omitted. The migration and tomography components can be directly computed within the adjoint modeling.

2.3. Direct envelope inversion (DEI)

Wu and Chen[31] proposed a direct envelope inversion (DEI) based on the energy scattering theory[42] to mitigate cycle skipping caused by lack of low-frequency components. With the strong scattering condition, the objective function for DEI focuses on the mismatch between the envelope transformed modeled data ($\mathbf{Env}[u]$) and observed data ($\mathbf{Env}[d]$):

$$J_{DEI}(\mathbf{m}) = \frac{1}{2}\sum_s\sum_r \int\left[\mathbf{Env}\left[u(t,m,r;s)\right] - \mathbf{Env}\left[d(t,r;s)\right]\right]^2 dt \tag{12}$$

where envelope transformed modeled data and observed data can be expressed as follows:

$$\begin{aligned} Env\left[u(t)\right] &= \sqrt{u^2(t) + \mathcal{H}[(u(t)]^2} \\ Env\left[d(t)\right] &= \sqrt{d^2(t) + \mathcal{H}[(d(t)]^2} \end{aligned} \tag{13}$$

The gradient for DEI can be derived from **Equation 12** with respect to model parameter $\mathbf{m}$:

$$\frac{\partial J_{DEI}(\mathbf{m})}{\partial \mathbf{m}} = \sum_s\sum_r \int \frac{\partial \mathbf{Env}\left[u(t,r;s)\right]}{\partial \mathbf{m}} \cdot \mathrm{R}_{DEI}(t,r;s) \tag{14}$$

where ($\partial\mathbf{Env}\left[u(t)\right]/\partial \mathrm{m}$) is defined as the partial derivative envelope wavefield, and $\mathrm{R}_{DEI} = \boldsymbol{Env}\left[u(t)\right] - \mathbf{Env}\left[d(t)\right]$ denotes the direct envelope residual. In the strong scattering approximation, the direct envelope virtual source can be written as follow:[31]

$$v_{DEI}(x,t) = \frac{1}{c(x)}\mathrm{G}_E(x,t;x_s) \tag{15}$$

where G_E denotes the envelope transformed Green's operator. Therefore, the reformulated DEI gradient is given by:

$$\mathrm{g}_{DEI} = \sum_s\sum_r \mathbf{v}_{DEI}(t) * \mathbf{B}_{DEI}(t) \tag{16}$$

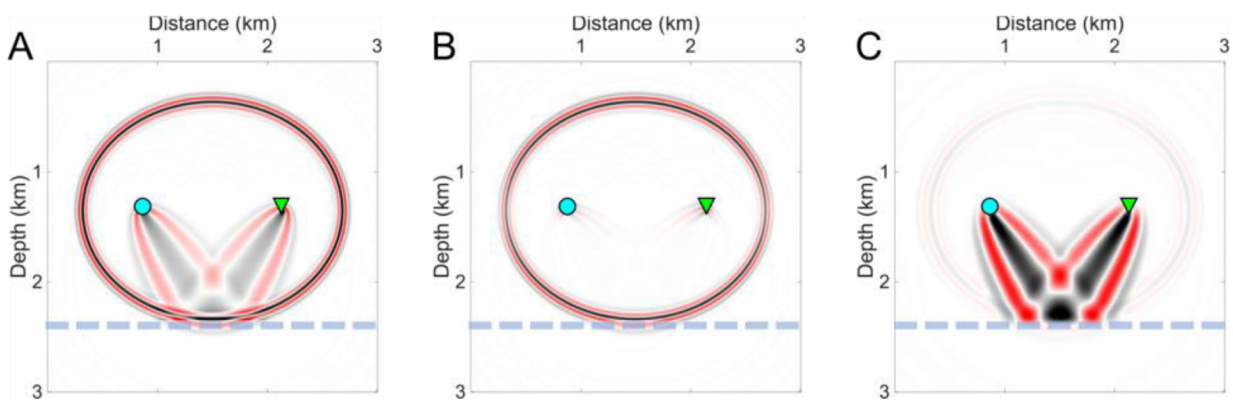

Figure 1. Comparison of the reflection kernels: (A) full reflection kernel, (B) migration, and (C) tomography component. The reflector, sources, and receivers are indicated by the dashed lines, cyan circles, and green triangles, respectively.

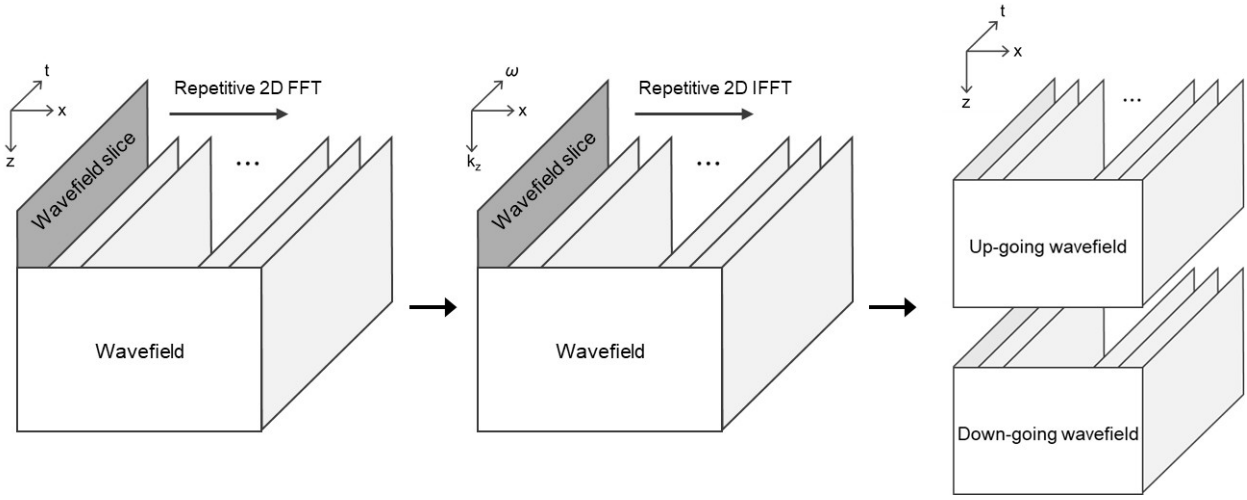

Figure 2. Schematic diagram of wavefield decomposition in f-k domain.
Abbreviations: 2D FFT: Two-dimensional fast Fourier transform; 2D IFFT: Two-dimensional inversefast Fourier transform.

where $\mathbf{v}_{DEI}(t)$ is the virtual source wavefield for DEI and $\mathbf{B}_{DEI}(t)$ is the adjoint source wavefield computed by propagating the time-reversed direct envelope residual.

2.4. Direct envelope–based RFWI (DE-RFWI)

Reflection full waveform inversion (RFWI) can reconstruct long-wavelength velocity models from reflection data by selectively utilizing tomography components. However, conventional RFWI suffers from cycle skipping when the data have insufficient low-frequency content.[25,28] To overcome this limitation, we propose the direct envelope-based RFWI (DE-RFWI) that incorporates the direct envelope into the RFWI. In coastal seismic surveys, operating sources that generate low-frequency energy is technically challenging. Under such shallow marine conditions, incorporating the direct envelope, which emphasizes energy distribution rather than waveform phase, allows long-wavelength information to be stably estimated from reflection data lacking low-frequency components.

Figure 3 shows the two-stage workflow of DE-RFWI process. The workflow consists of the first stage that creates reflectors and the second stage that updates the long-wavelength velocity models. By using the Hilbert transform based decomposition method, the desired component at each stage can be directly obtained during the adjoint modeling without additional 2D FFT operations. Since subsurface information is usually limited, the initial velocity model does not contain reflectors, which hinders the formation of the rabbit-ear-shaped tomography kernel. Therefore, in the first stage, the migration component in **Equation 10** is used to update a temporary short-wavelength model. The short-wavelength model is used as the initial model for the second stage.

In the second stage, an envelope-based objective function is employed to recover the long-wavelength velocity models, and the tomography components are extracted accordingly. According to the **Equations 11** and **16**, the tomography component of DE-RFWI can be expressed as follows:

$$g_{tomo} = \sum_s \sum_r 2\left[\mathbf{v}_{DEI}(t) * \mathbf{B}_{DEI}(t) - \mathcal{H}_z\left[\mathbf{v}_{DEI}(t)\right] * \mathcal{H}_z\left[\mathbf{B}_{DEI}(t)\right]\right] \quad (17)$$

The tomography component is accumulated into the initial model at each iteration, whereas the short-wavelength temporary model is discarded. The updated long-wavelength model is used as the initial model for the first stage of the next iteration.

3. Numerical examples

3.1. Synthetic test

In this part of numerical example, we conducted a synthetic test on the survey conditions of a short-offset marine acquisition. This test was carried out to verify the performance of the proposed DE-RFWI and to compare the results with obtained from conventional FWI and RFWI. The velocity model used in this test has a 30 m water depth and includes an ellipse-shaped anomaly (Figure 4A). The receiver offset range is 18–87 m, with a group interval of 3 m. Assuming a vessel speed of 4 knots and a shooting interval of 2 s, the shot interval is 4 m, and the recording time is 0.3 s. These survey parameters were considered to simulate the shallow marine survey conditions. The initial velocity model is shown in Figure 4B, and a Ricker wavelet with a cutoff frequency of 100 Hz was used as the source

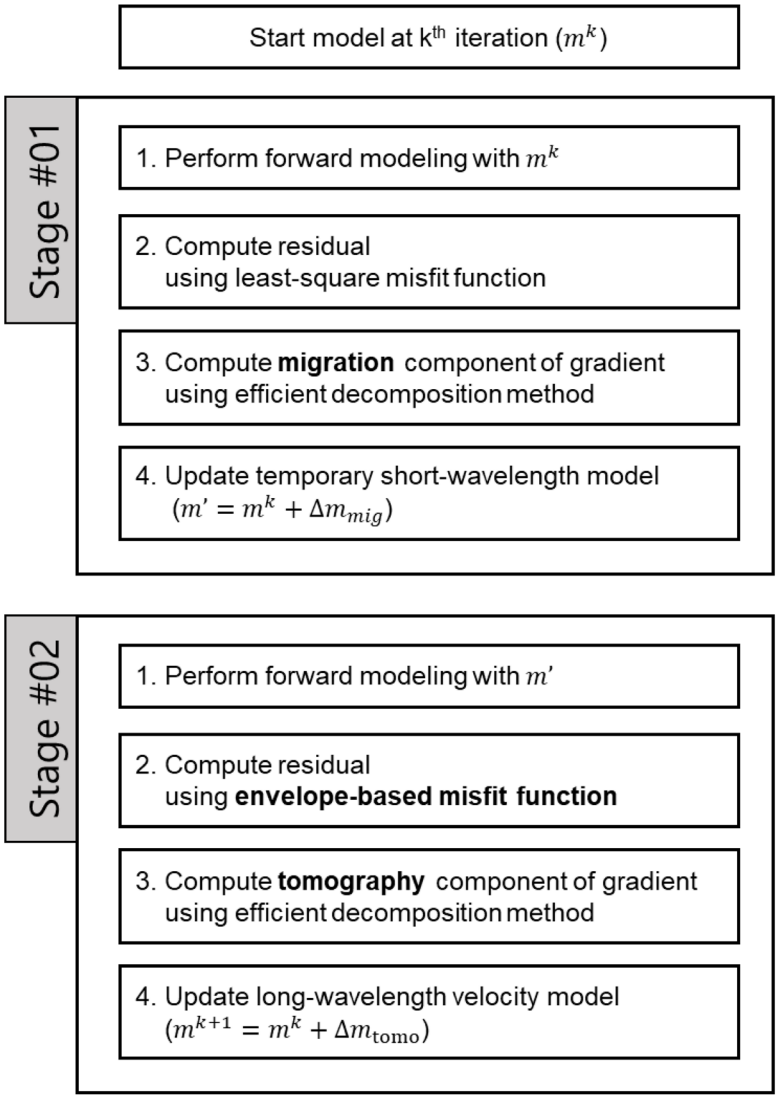

Figure 3. Two-stage workflow of the DE-RFWI process
Abbreviation: DE-RFWI: Direct envelope–based reflection full waveform inversion.

wavelet (Figure 5). The bandwidth and recording time in this test are consistent with typical shallow high-resolution survey parameters and the geometry of the field data. Forward modeling was carried out using the 2D acoustic wave equation under the assumption of constant density.

Since the maximum offset range is insufficient to record wide-aperture signals, most of the recorded energy consists of reflections. To verify the DE-RFWI, we compared the performance with that of conventional FWI and RFWI. Figure 6 depicts the comparison of the inversion results. For FWI, the lack of wide-aperture information leads to updates that are primarily confined to reflector boundaries, and the reflector velocities are not completely recovered (Figure 6A). RFWI also fails to reconstruct the long-wavelength velocity (Figure 6B), because the limited offset causes the migration component to dominate, leaving the separated tomography component would be still dominant by migration energy. However, the DE-RFWI yields a stable long-wavelength velocity (Figure 6C). Especially, whereas RFWI produces localized updates near the upper and lower edges of the anomaly, DE-RFWI achieves a more spatially distributed and consistent update throughout the model.

These results are also demonstrated on the velocity profiles (Figure 7). DE-RFWI provides a more stable estimation of the long-wavelength velocity compared with

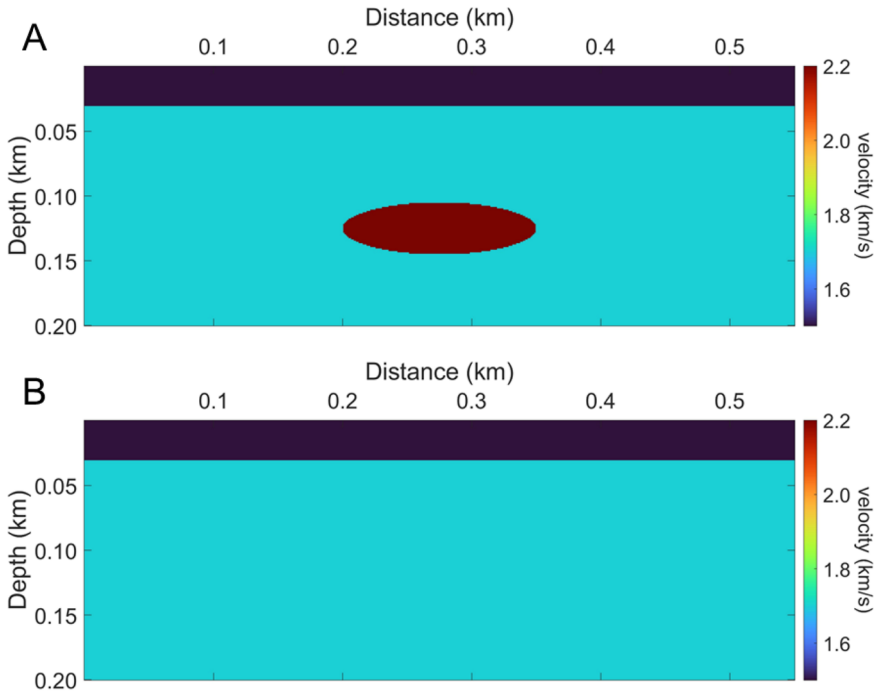

Figure 4. (A) True velocity model and (B) initial velocity model for synthetic test

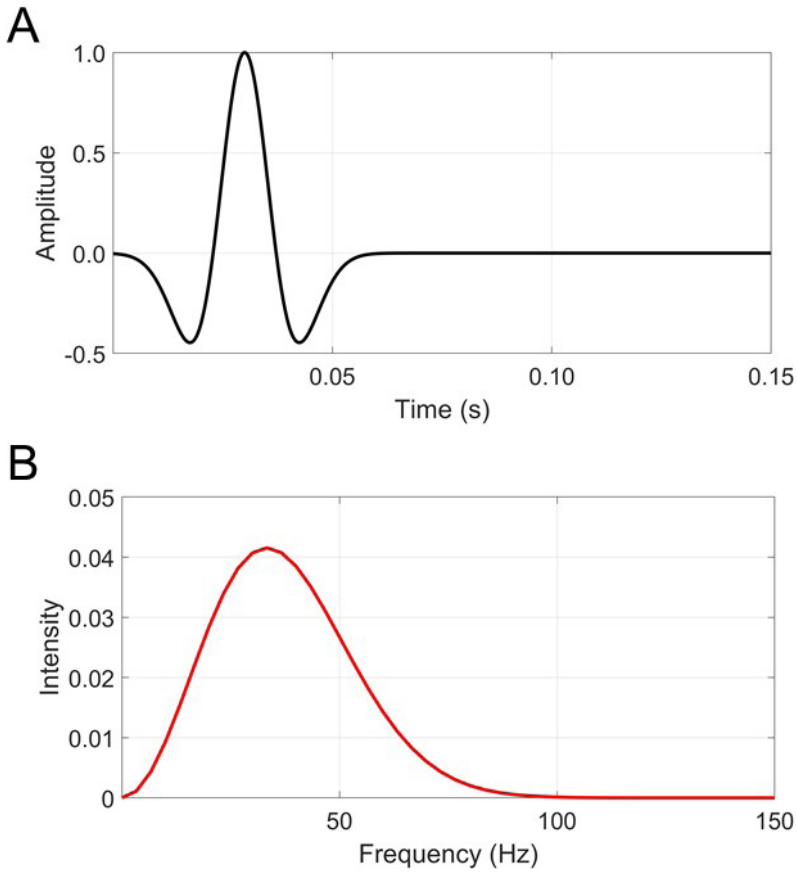

Figure 5. Ricker wavelet with a cutoff frequency of 100 Hz used in (A) synthetic test, and (B) its frequency spectrum

the FWI and RFWI results. Because FWI and RFWI fail to recover the background velocity, the updates occur at position shallower than the actual lower reflector, which is a consequence of the waveform-matching objective functions. However, DE-RFWI was able to reconstruct the long-wavelength velocity. Therefore, the synthetic example on the shallow marine survey demonstrates that the proposed DE-RFWI method can yield a more reliable long-wavelength velocity model with limited offsets.

3.2. Field data application

To verify the field applicability, we conducted DE-RFWI to seismic data acquired in Yeongil Bay, South Korea. Figure 8 shows the survey area, where water depth is less than 30 m. In the coastal region, the shallow towing depth of the source and receivers makes the direct signal highly susceptible to contamination by irregular sea-surface reflections. Thus, source estimation based on direct signals becomes unstable. In this study, we estimated the source signature using seafloor reflections, which can be recorded more reliably at short offsets. However, the use of seafloor reflections requires a reliable near-seafloor velocity model. Accordingly, we adopted the velocity model obtained from refraction tomography conducted in the same survey area.

The source equipment was an air-gun manufactured by Bolt with a chamber volume of 10 in^3. It was fired in a time-

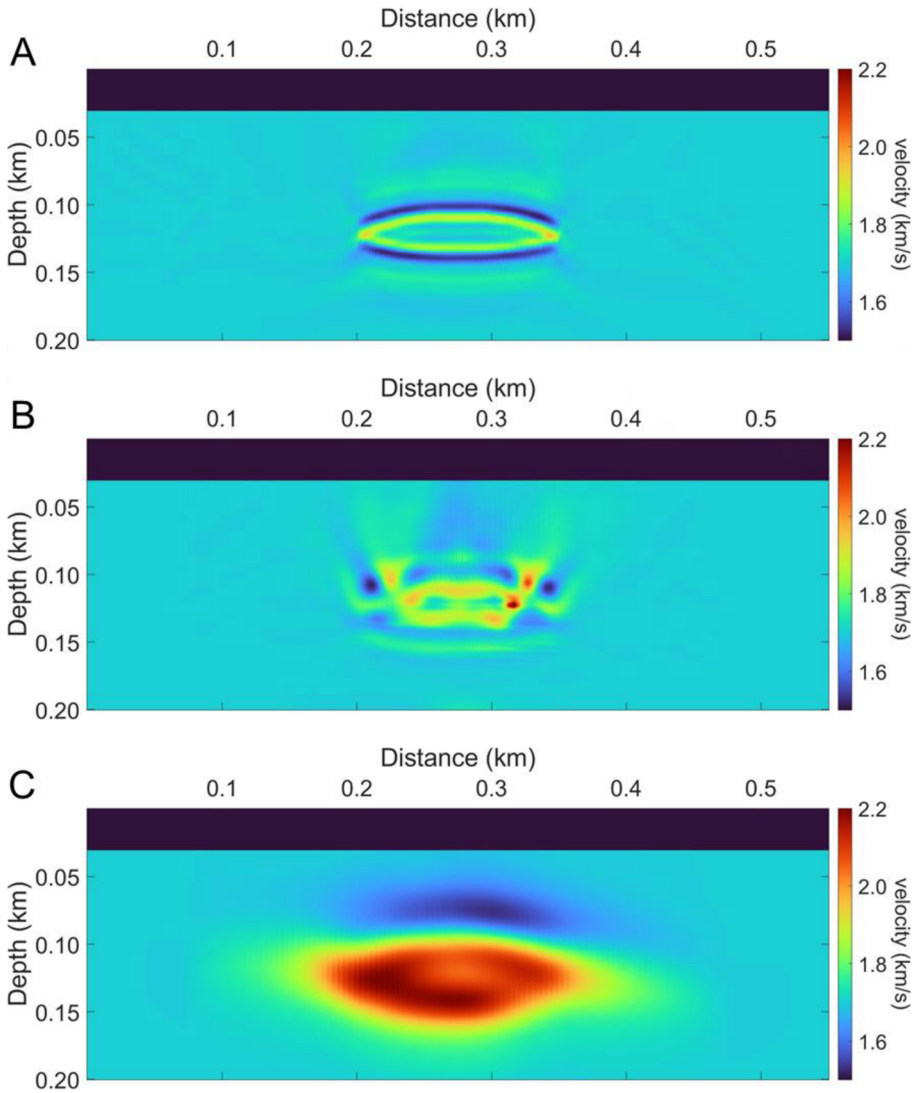

Figure 6. Comparison of results on (A) FWI, (B) RFWI, and (C) DE-RFWI
Abbreviations: DE-RFWI: Direct envelope–based reflection full waveform inversion; FWI: Full waveform inversion; RFWI: Reflection full waveform inversion.

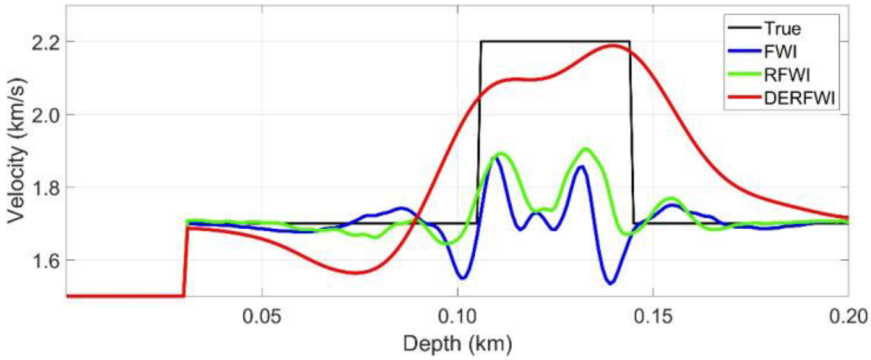

Figure 7. Comparison of velocity profiles extracted at the distance of 0.27 km: the true velocity (black), FWI (blue), RFWI (green), and DE-RFWI (red) Abbreviations: DE-RFWI: Direct envelope–based reflection full waveform inversion; FWI: Full waveform inversion; RFWI: Reflection full waveform inversion.

shooting method at 2 s intervals, corresponding to a shot spacing of approximately 4 m at an average vessel speed of about 4 knots. Totally, 2335 shots were recorded, of which 1000 shots were used for inversion. The receiver was a 24-channel streamer manufactured by SIG, with a group interval of 3.125 m. The offset range was about 18–90 m. The recording length was 0.2 s, and the sampling interval was 100 μs.

Pre-processing is essential to ensure the signal quality before applying field data to inversion. The trigger time between the source controller and receiver unit directly affects the temporal alignment of the recorded waveforms. A mismatch of trigger time can cause events to be delayed or recorded prematurely, leading to incorrect interpretation. In air-gun surveys, a gun-delay exists between the trigger signal generated by the air-gun controller and the actual firing, and the delay was compensated to synchronize the trigger time.

The field data contain various mechanical and electrical noises, requiring additional noise suppression procedures. In this study, high frequency noise components above 200 Hz were removed through low-pass filtering. The direct signals were muted because direct waves can be easily contaminated by irregular sea-surface reflections in shallow coastal zones. Figure 9 presents the near-offset gather and representative common shot gather after the pre-processing, and complex reflection events can be clearly observed.

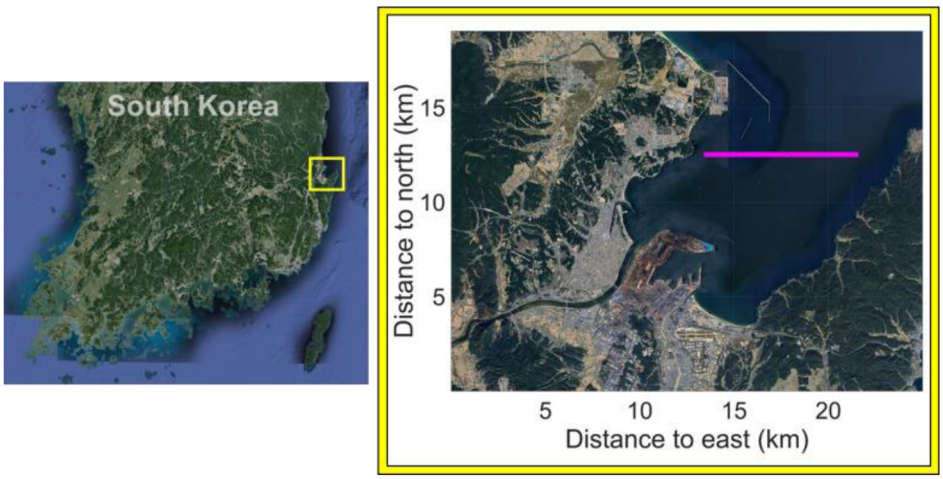

Figure 8. Survey area in Yeongil Bay, Sourth Korea. The survey line is indicated by a magenta line.

For field data inversion where subsurface information is limited, an initial velocity model that linearly increases with depth is widely used. In this study, we modified model to enhance the stability of the inversion by incorporating the observed characteristics of data into the initial model. Owing to the short offset and high frequency bandwidth, the data are of high resolution (Figure 9). The near-offset gather data reveals a sedimentary structure beneath the seafloor after distance of 1.8 km (Figure 9A). The two-way travel time of the reflection occurring below the seafloor reflection is approximately 0.04 s. The shallow subsurface in this region is known to consist of marine sand deposits.[43] Accordingly, instead of a simple linearly increasing velocity model, we constructed the initial model by incorporating the geomorphological features observed in the data (Figure 10A).

We carried out inversion using the modified linearly increasing model (Figure 10A) and the tomography model (Figure 10B) as initial model. Figure 11 shows the inversion results for each initial model. Although the tomography model that contains travel-time information is a relatively favorable velocity model, both results exhibit similar trends. This demonstrates that the proposed DE-RFWI can stably reconstruct long-wavelength velocity even under poor initial models.

According to the inversion results, the vertical and horizontal velocity variations are improved (Figure 11). In particular, the complex velocity structure shallower than 0.12 km is successfully recovered. Moreover, the distribution of low-velocity zones around the distance of 3.0 km and 3.5 km indicates enhanced structural resolution relative to the initial model (Figure 11B). The results of inversion demonstrate that the DE-RFWI can effectively and stably update long-wavelength velocity models when applied to short-offset data acquired in shallow water depth. However, the velocity structure below 0.1 km depth may be inaccurate. It is because the maximum offset range of the field data (0.1 km) is insufficient to adequately constrain deeper velocities, and the relatively small chamber size of air-gun may have caused signal attenuation.

To validate the result of DE-RFWI, a comparison of the observed and modeled data generated from Figure 11B was conducted using representative traces. In shallow marine conditions, the recorded data are dominated by strong reflections (Figure 9). However, since the DE-RFWI reconstructs the long-wavelength components of the velocity model, direct amplitude-based comparison is not appropriate. The long-wavelength components mainly affect travel time; therefore, we evaluated the inversion result by analyzing the arrival-time alignment between the observed and modeled data.

Figure 12 presents the windowed and their enveloped traces to analyze the arrival time alignment. For focus on the later signals, a time window after the seafloor primary reflection was applied (0.065–0.16 s). Figure 12A shows the comparison of observed and modeled traces at a shot position of 1.82 km, presented in relative amplitude. This location corresponds to the interval where sedimentary structures begin to appear from the survey line of 1.9 km (Figure 9). The relative amplitude of the signals observed at approximately 0.08 s is reasonably reproduced in the modeled trace. Figure 12B presents the envelope traces of Figure 12A. The blue boxes indicate the envelope peaks of the observed data. Comparison with the modeled envelope

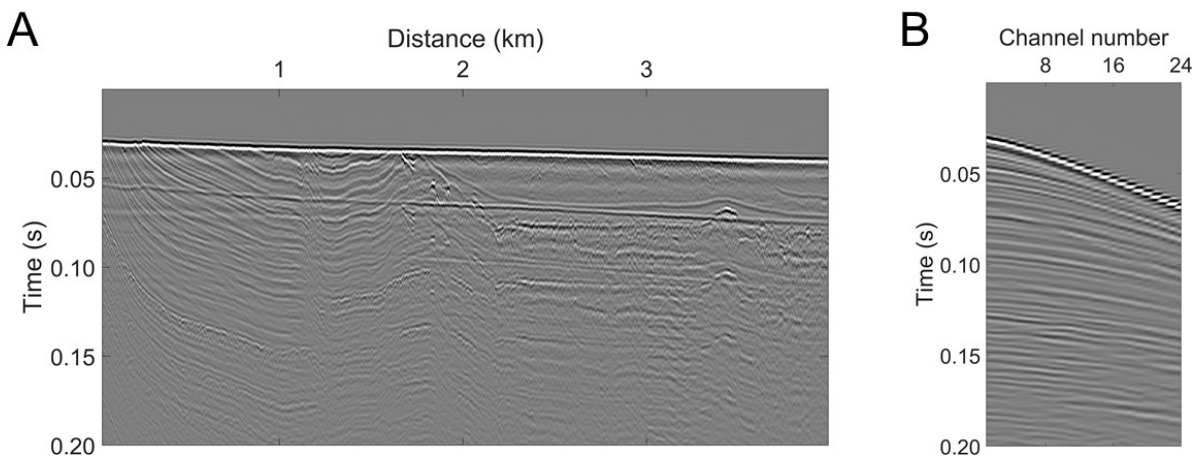

Figure 9. (A) Pre-processed near-offset gather and (B) representative common shot gather of field seismic data

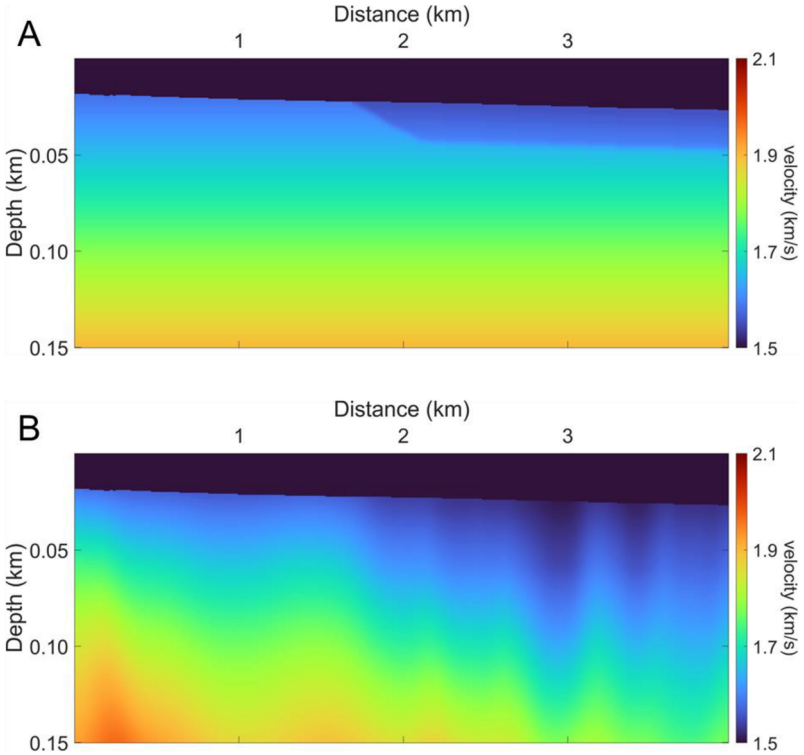

Figure 10. Comparison of the initial velocity models: (A) modified linearly increasing model, and (B) tomography model

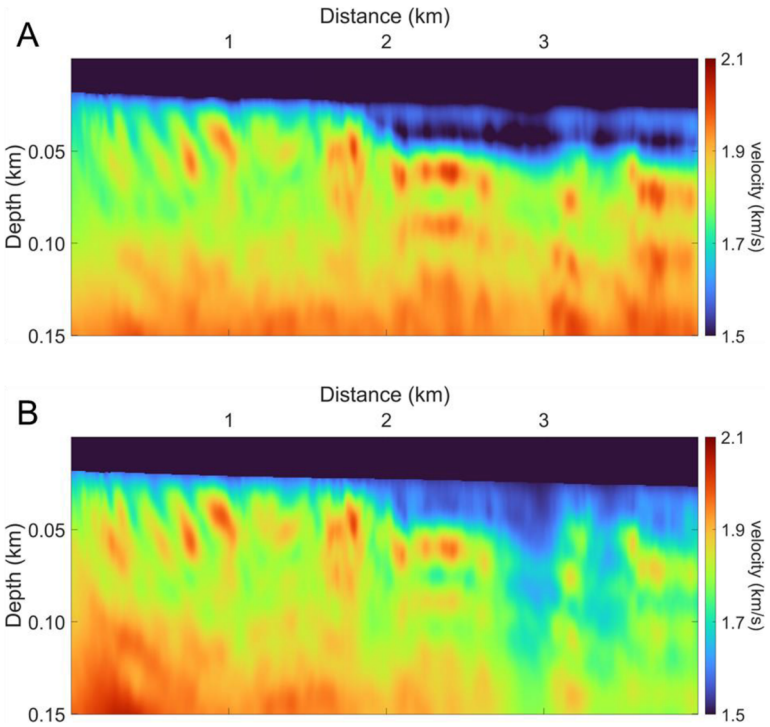

Figure 11. Comparison of the inverted velocities using initial model as (A) modified linearly increasing model (Figure 9A) and (B) tomography model (Figure 9B)

peak demonstrates that the arrival time of the main peaks is generally aligned.

Figure 12C displays the trace comparison of a shot position of 2.9 km. This location lies in the area influenced by the sedimentary structure. Compared with Figure 12A, the reference reflection event is observed at delayed time by the structural effect shown in inverted result (Figure 11). The reproduced relative amplitude trend can be observed (Figure 12C). Figure 12D depicts the envelope transformed data of Figure 12C. The envelope peaks within the 0.09–0.12 s are generally aligned. However, discrepancies can be detected after 0.12 s.

In this section, the result of DE-RFWI were evaluated based on relative amplitudes of windowed traces and arrival time alignment in the envelope domain. The relative amplitudes and peak-to-peak alignment are generally consistent, although additional peaks that are not clearly observed in the field data are presented in the modeled result.

Since the well-log data is not available for the Yeongil Bay field data, the inverted velocity should be verified by indirect approach. To verify the inverted velocity, a comparison of reverse time migration (RTM) was performed. Figure 13A demonstrates the RTM result using the initial velocity model in Figure 10B, whereas Figure 13B presents the RTM result derived from the inverted velocity model in Figure 11B. The green arrows indicate the improvements in the migration results. The RTM result using inverted velocity with DE-RFWI exhibits a markedly improved continuity of reflection events. Especially, the horizontal reflection around a distance of 2 km is imaged in a flattened and coherent event. These enhanced imaging results demonstrate that the proposed DE-RFWI approach can reliably and accurately reconstruct long-wavelength velocity models when applied to field data.

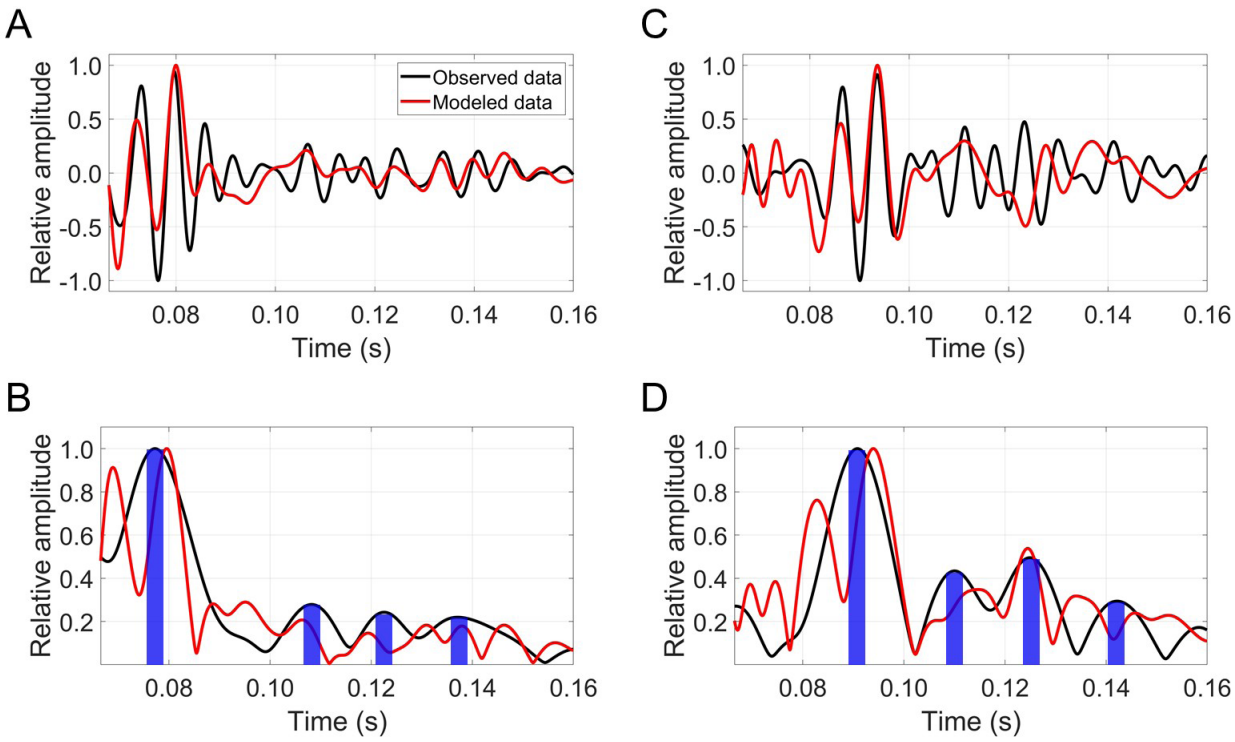

Figure 12. Trace comparison for relative amplitude trend and arrival-time alignment analysis: (A) First channel traces of shot located at 1.82 km, (B) envelope traces of (A), (C) first channel traces of shot located at 2.9 km, and (D) envelope traces of (C). Blue vertical bars indicate the envelope peak positions of the observed data.

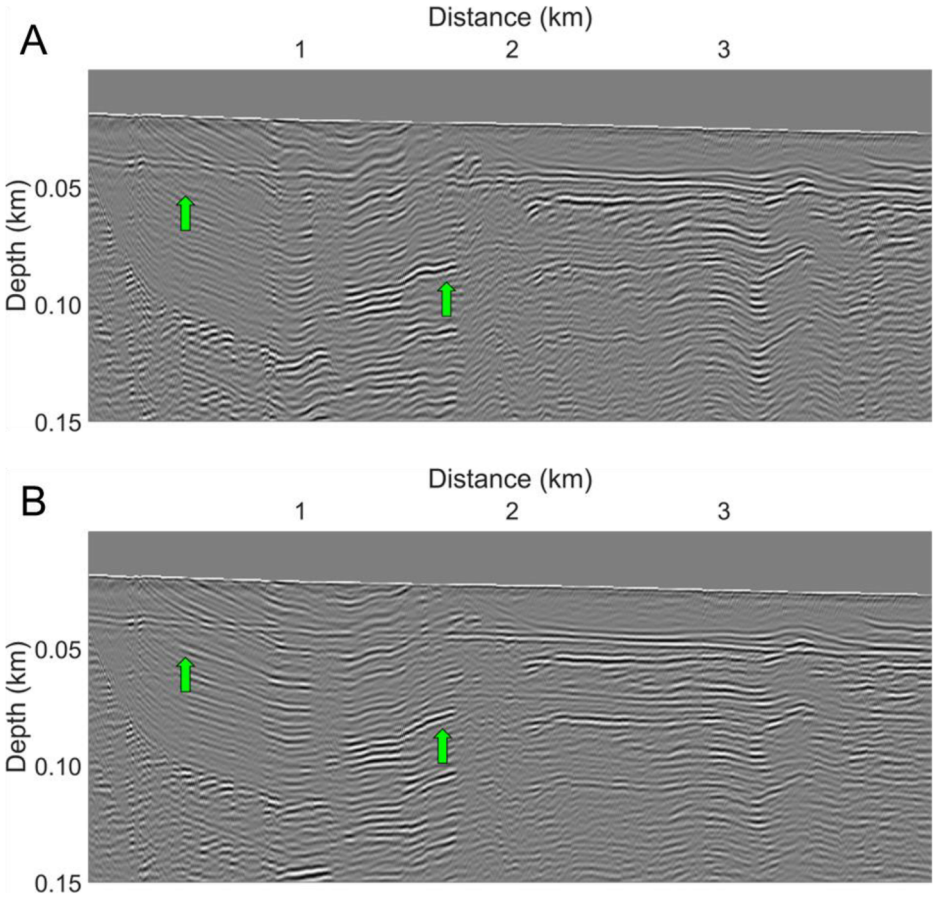

Figure 13. Comparison of the migration results. (A) Using the initial tomography model (Figure 10B) and (B) the inverted velocity model using DE-RFWI (Figure 11B). The green arrows indicate representative improvements.
Abbreviations: DE-RFWI: Direct envelope–based reflection full waveform inversion.

4. Conclusion

Shallow marine seismic data is characterized by short offsets and reflection dominance. Although RFWI has been proposed to recover long-wavelength velocity from reflection data, it remains susceptible to cycle skipping when low-frequency components are insufficient. To overcome this, we propose DE-RFWI, which incorporates the direct envelope into the RFWI to contribute to the reconstruction of long-wavelength velocity. Wavefield decomposition method to separate gradient into migration and tomography component performed in frequency-wavenumber domain requires repeated 2D FFT and storing of source and receiver wavefield at every time step, leading to high computational cost. This limitation is particularly critical in shallow marine seismic data. Therefore, we employed a Hilbert transform-based implicit decomposition method performed in time-space domain. The results of numerical examples to both synthetic and field data from Yeongil Bay, South Korea demonstrate that DE-RFWI successfully reconstructs long-wavelength velocity models, even with poor initial models. In the field data example, the inversion results show consistent arrival-time alignment and related amplitude trends in later time. The velocity model obtained from DE-RFWI also improves reflector continuity and resolution in RTM images. These results indicate that DE-RFWI is an effective approach for building reliable long-wavelength velocity models in shallow marine seismic data. In addition, proposed method is expected to support high-resolution velocity model and contribute to geotechnical assessment and engineering design in marine environments.

Acknowledgments

We thank Dr. Sumin Kim and Principal Engineer Gabseok Seo for their insightful comments and technical expertise, which greatly improved the quality of this article.

Funding

This work was supported by the Basic Research Project "Development of operation management infrastructure for TAMHAE3 and seamless seismic technology connecting coastal areas (26-3322)" of the Korea Institute of Geoscience and Mineral Resources (KIGAM) funded by the Ministry of Science and ICT of Korea.

Conflict of interest

The authors declare that there are no conflicts of interest or competing interests.

Author contributions

Conceptualization: Kyoungmin Lim, Jiho Ha
Formal analysis: Wookeen Chung, Jungkyun Shin
Investigation: Kyoungmin Lim, Jiho Ha, Jungkyun Shin
Methodology: Kyoungmin Lim, Jiho Ha
Supervision: Jiho Ha
Validation: Wookeen Chung
Visualization: Kyoungmin Lim
Writing–original draft: Kyoungmin Lim, Jiho Ha
Writing–review & editing: All authors

Availability of data

All data analyzed have been presented in the paper.

References

1. Prager BT, Caughey DA, Poeckert RH. Bottom classification: operational results from QTC VIEW. In: *Proceedings of the Challenges of Our Changing Global Environment.* OCEANS '95 MTS/IEEE; October 9-12, 1995; San Diego, CA, USA. 1995;3:1827-1835.

   doi: 10.1109/OCEANS.1995.528859

2. Mair E, Parnum I, Schut T. Using multibeam echo-sounder backscatter to characterise the seafloor of Davis Harbour, Antarctica: Preliminary results. In: *Proceedings of the Acoustics 2012 – Fremantle: Acoustics, Development, and the Environment.* The 2012 Conference of the Australian Acoustical Society; November 21-23, 2012; Fremantle, Australia. Australian Acoustical Society; 2012.

3. Viala C, Lamouret M, Abadie A. Seafloor classification using a multibeam echo sounder: A new rugosity index coupled with a pixel-based process to map Mediterranean marine habitats. *Appl Acoust*. 2021;179:108067.

   doi: 10.1016/j.apacoust.2021.108067

4. Brookshire BN Jr, Landers FP, Stein JA. Applicability of ultra-high-resolution 3D seismic data for geohazard identification at mid-slope depths in the Gulf of Mexico: Initial results. *Underw Technol.* 2015;32(4):271-278.

   doi: 10.3723/ut.32.271

5. Shin J, Ha J, Kang NK, Kim HD, Kim CS. Development of a portable 3D seismic survey system for nearshore surveys and the first case study offshore Pohang, South Korea. *Mar Geophys Res*. 2021;42(4):34.

   doi: 10.1007/s11001-021-09453-x

6. Luo Y, Schuster GT. Wave-equation traveltime inversion. *Geophysics*. 1991;56(5):645-653.

   doi: 10.1190/1.1443081

7. Zelt CA, Smith RB. Seismic traveltime inversion for 2-D crustal velocity structure. *Geophys J Int*. 1992;108(1):16-34.

   doi: 10.1111/j.1365-246x.1992.tb00836.x

8. Ravaut C, Operto S, Improta L, Virieux J, Herrero A, Dell'Aversana P. Multiscale imaging of complex structures from multifold wide-aperture seismic data by frequency-domain full-waveform tomography: application to a thrust belt. *Geophys J Int*. 2004;159(3):1032-1056.

   doi: 10.1111/j.1365-246x.2004.02442.x

9. Pichot T, Delescluse M, Chamot-Rooke N, *et al*. Deep crustal structure of the conjugate margins of the SW South China Sea from wide-angle refraction seismic data. *Mar Pet Geol*. 2014;58:627-643.

   doi: 10.1016/j.marpetgeo.2013.10.008

10. Mora P. Inversion = migration + tomography. *Geophysics*. 1989;54(12):1575-1586.

    doi: 10.1190/1.1442625

11. Virieux J, Operto S. An overview of full-waveform inversion in exploration geophysics. *Geophysics*. 2009;74(6):WCC1-WCC26.

    doi: 10.1190/1.3238367

12. Zhou W, Brossier R, Operto S, Virieux J. Full waveform inversion of diving and reflected waves for velocity model building with impedance inversion based on scale separation. *Geophys J Int*. 2015;202(3):1535-1554.

    doi: 10.1093/gji/ggv228

13. Xu S, Wang D, Chen F, Lambaré G, Zhang Y. Inversion on Reflected Seismic Wave. In: *Proceedings of the SEG Technical Program Expanded Abstracts 2012.* 82th SEG Annual International Meeting; November 4-9, 2012; Las Vegas, Nevada, USA. Society of Exploration Geophysicists; 2012:1-7.

    doi: 10.1190/segam2012-1473.1

14. Tang Y, Lee S, Baumstein A, Hinkley D. Tomographically enhanced full wavefield inversion. In: *Proceedings of the SEG Technical Program Expanded Abstracts 2013.* 83th SEG Annual International Meeting; September 22-27, 2013; Houston, Texas, USA. Society of Exploration Geophysicists; 2013:1037-1041.

    doi: 10.1190/segam2013-1145.1

15. Alkhalifah T. Scattering-angle based filtering of the waveform inversion gradients. *Geophys J Int*. 2015;200(1):363-373.

doi: 10.1093/gji/ggu379

16. Wang F, Donno D, Chauris H, Calandra H, Audebert F. Waveform inversion based on wavefield decomposition. *Geophysics*. 2016;81(6):R457-R470.

doi: 10.1190/geo2015-0340.1

17. Yao G, da Silva NV, Warner M, Kalinicheva T. Separation of Migration and Tomography Modes of Full-Waveform Inversion in the Plane Wave Domain. *J Geophys Res Solid Earth*. 2018;123(2):1486-1501.

doi: 10.1002/2017jb015207

18. Guo Q, Alkhalifah T. Elastic reflection-based waveform inversion with a nonlinear approach. *Geophysics*. 2017;82(6):R309-R321.

doi: 10.1190/geo2016-0407.1

19. Li Y, Alkhalifah T. Multi-parameter reflection waveform inversion for acoustic transversely isotropic media with a vertical symmetry axis. *Geophys Prospect*. 2020;68(6):1878-1892.

doi: 10.1111/1365-2478.12966

20. Wu S, Wang T, Cheng J. Second-order optimization for multiparameter reflection waveform inversion in acoustic VTI media. *Geophys J Int*. 2024;236(1):249-269.

doi: 10.1093/gji/ggad406

21. Song C, Alkhalifah T. A reflection-based efficient wavefield inversion. *Geophysics*. 2021;86(4):R497-R508.

doi: 10.1190/geo2019-0664.1

22. Wang T, Cheng J, Geng J. Reflection full waveform inversion with second-order optimization using the adjoint-state method. *J Geophys Res Solid Earth*. 2021;126(8):e2021.

doi: 10.1029/2021jb022135

23. Xu W, Hu G, He B, Du Z. Seismic reflection waveform inversion based on Gauss–Newton optimization. *J Geophys Eng*. 2022;19(4):846-862.

doi: 10.1093/jge/gxac053

24. Xu S, Chen F, Lambaré G, Zhang Y. Full waveform inversion of reflected seismic data. *J Seism Explor*. 2013;22(5):449-462.

25. Wang S, Chen F, Zhang H, Shen Y. Reflection-based full waveform inversion (RFWI) in the frequency domain. In: *Proceedings of the SEG Technical Program Expanded Abstracts 2013*. 83th SEG Annual International Meeting; September 22-27, 2013; Houston, Texas, USA. Society of Exploration Geophysicists; 2013:877-881.

doi: 10.1190/segam2013-0671.1

26. Wang P, Zhang Z, Wei Z, Huang R. A demigration-based reflection full-waveform inversion workflow. In: *Proceedings of the SEG Technical Program Expanded Abstracts 2018*. 88th SEG Annual International Meeting; October 14-19, 2018; Anaheim, California, USA. Society of Exploration Geophysicists; 2018:1138-1142.

doi: 10.1190/segam2018-2997404.1

27. Yao G, Wu D, Wang SX. A review on reflection-waveform inversion. *Pet Sci*. 2020;17(2):334-351.

doi: 10.1007/s12182-020-00431-3

28. Chi B, Dong L, Liu Y. Correlation-based reflection full-waveform inversion. *Geophysics*. 2015;80(4):R189-R202.

doi: 10.1190/geo2014-0345.1

29. Chen G, Wu R, Chen S. Reflection multi-scale envelope inversion. *Geophys Prospect*. 2018;66(7):1258-1271.

doi: 10.1111/1365-2478.12624

30. Wang Y, Chi B, Dong L. Envelope normalized reflection waveform inversion. *Geophys Prospect*. 2024;73(3):895-909.

doi: 10.1111/1365-2478.13598

31. Wu RS, Chen GX. Multi-scale seismic envelope inversion using a direct envelope Frechet derivative for strong-nonlinear full waveform inversion. *arXiv*. Preprint posted online August 15, 2018. Accessed March 19, 2026.

doi: 10.48550/arXiv.1808.05275

32. Chen GX, Wu RS, Chen SC. Multiscale Direct Envelope Inversion: Algorithm and Methodology for Application to the Salt Structure Inversion. *Earth Space Sci*. 2019;6(1):174-190.

doi: 10.1029/2018EA000453

33. Luo J, Wu RS, Chen G. Angle domain direct envelope inversion method for strong scattering velocity and density estimation. *IEEE Geosci Remote Sens Lett*. 2020;17(9):1508-1512.

doi: 10.1109/LGRS.2019.2950471

34. Lee D, Kang SG, Kim S, Kim YS, Chung W. Efficient direct envelope inversion with excitation amplitude for strong velocity contrast model. *IEEE Trans Geosci Remote Sens*. 2024;62:1-12.

doi: 10.1109/TGRS.2024.3422978

35. Lian S, Yuan S, Wang G, Liu T, Liu Y, Wang S. Enhancing low-wavenumber components of full-waveform inversion using an improved wavefield decomposition method in the time-space domain. *J Appl Geophys*. 2018;157:10-22.

doi: 10.1016/j.jappgeo.2018.06.013

36. Jun H. Frequency-domain reflection-based full waveform inversion for short-offset seismic data. *J Appl Geophys*. 2019;164:106-116.

doi: 10.1016/j.jappgeo.2019.03.010

37. Wu Z, Alkhalifah T. Simultaneous inversion of the background velocity and the perturbation in full-waveform

inversion. *Geophysics*. 2015;80(6):R317-R329.

doi: 10.1190/geo2014-0365.1

38. Tarantola A. Inversion of seismic reflection data in the acoustic approximation. *Geophysics*. 1984;49(8):1259-1266.

doi: 10.1190/1.1441754

39. Pratt RG, Shin C, Hicks GJ. Gauss-Newton and full Newton methods in frequency-space seismic waveform inversion. *Geophys J Int*. 1998;133(2):341-362.

doi: 10.1046/j.1365-246x.1998.00498.x

40. Hu LZ, McMechan GA. Wave-field transformations of vertical seismic profiles. *Geophysics*. 1987;52(3):307-321.

doi: 10.1190/1.1442305

41. Fei TW, Luo Y, Yang J, Liu H, Qin F. Removing false images in reverse time migration: The concept of de-primary. *Geophysics*. 2015;80(6):S237-S244.

doi: 10.1190/geo2015-0289.1

42. Wu RS. Multiple scattering and energy transfer of seismic waves — separation of scattering effect from intrinsic attenuation — I. Theoretical modelling. *Geophys J Int*. 1985;82(1):57-80.

doi: 10.1111/j.1365-246x.1985.tb05128.x

43. Ha J, Shin J, Lim K, Um IK, Yi B. 3D UHR seismic and back-scattering analysis for seabed and ultra-shallow subsurface classification. *Acta Geophys*. 2024;73(2):1363-1376.

doi: 10.1007/s11600-024-01423-2